INTERNATIONAL JOURNAL FOR NUMERICAL METHODS IN FLUIDS
Int. J. Numer. Meth. Fluids 2003; **42**:665–693 (DOI: 10.1002/fld.551)

A time-implicit high-order compact differencing and filtering scheme for large-eddy simulation

D. P. Rizzetta[1,*,†], M. R. Visbal[1] and G. A. Blaisdell[2]

[1]*Air Force Research Laboratory, Wright-Patterson Air Force Base, OH 45433-7521, U.S.A.*
[2]*Purdue University, West Lafayette, IN 47907-1282, U.S.A.*

SUMMARY

This work investigates a high-order numerical method which is suitable for performing large-eddy simulations, particularly those containing wall-bounded regions which are considered on stretched curvilinear meshes. Spatial derivatives are represented by a sixth-order compact approximation that is used in conjunction with a tenth-order non-dispersive filter. The scheme employs a time-implicit approximately factored finite-difference algorithm, and applies Newton-like subiterations to achieve second-order temporal and sixth-order spatial accuracy. Both the Smagorinsky and dynamic subgrid-scale stress models are incorporated in the computations, and are used for comparison along with simulations where no model is employed. Details of the method are summarized, and a series of classic validating computations are performed. These include the decay of compressible isotropic turbulence, turbulent channel flow, and the subsonic flow past a circular cylinder. For each of these cases, it was found that the method was robust and provided an accurate means of describing the flowfield, based upon comparisons with previous existing numerical results and experimental data. Published in 2003 by John Wiley & Sons, Ltd.

KEY WORDS: high-order numerical method; large-eddy simulation; compact finite-difference scheme; subgrid-stress model

1. INTRODUCTION

Due to severe resolution requirements resulting in excessive expenditure of computational resources, direct-numerical simulation (DNS) of turbulent flows is generally limited to relatively low Reynolds numbers and to simple geometric configurations. In order to reduce these demands, particularly for practical applications, it is desirable to model certain aspects of the turbulence in some manner. This has been difficult because the large-scale structures, which contain most of the turbulent energy, vary considerably from one flow to another, thereby

*Correspondence to: D. P. Rizzetta, AFRL/VAAC, Building 146-Room 225, 2210 Eighth Street, Wright-Patterson AFB, OH 45433-7521, U.S.A.
†E-mail: donald.rizzetta@afrl.af.mil

Contract/grant sponsor: U.S. Air Force Office of Scientific Research; contract/grant number: Task 2307AW
Contract/grant sponsor: U.S. Department of Defence Major Shared Resource Centres

Received 17 April 2002
Revised 3 March 2003

precluding a general description. In large-eddy simulation (LES), only the small-scale structures are left unresolved and must be accounted for through use of a subgrid-scale (SGS) turbulence model. LES thus extends the class of flows that can be simulated for a given amount of computational resources beyond those of DNS. Also, since the small-scale structures are believed to be homogeneous and possess a universal character, they may be more easily and reliably modelled. Additionally, the small structures contain only a fraction of the total turbulent kinetic energy, and therefore it is generally assumed that they may be accounted for without unduly affecting the large eddies.

The oldest and most popular subgrid-stress model is the formulation due to Smagorinsky [1], in which an eddy viscosity is assumed to be proportional to the product of the local large-scale strain rate and the square of the local grid scale. The coefficient of proportionality is commonly taken to be a constant, but its value must be adjusted a priori for each specific application. Several attempts have been made to improve the Smagorinsky model, and it has been applied successfully, both in its original and modified forms, to a number of simulations that include decaying isotropic turbulence [2], turbulent planar channel flows [3–7], compressible turbulent flows [8, 9], and turbulent mixing layers [10]. These computations and others have identified the following major deficiencies of the Smagorinsky model: (1) the eddy viscosity constant is flow dependent, (2) limiting behaviour near solid boundaries and in laminar regimes is incorrect, (3) the model does not account for the backscatter of energy from small to large scales [11], (4) the model is overly dissipative, and (5) the model does not account for compressibility effects [9].

More recent large-eddy simulations have been performed employing the dynamic subgrid-scale model of Germano *et al.* [12]. The major advantage of this model is that it adjusts to local flow conditions by using the resolved large-scale information to predict the effects of the small-scale structures. It thus has the potential for treating more complex flows by LES than was previously possible. The dynamic model allows for the proper behaviour near solid surfaces or in laminar regions, and does not preclude the backscatter of turbulent energy, providing improvement over a less sophisticated approach. The original model was extended for use in compressible flows by Moin *et al.* [13], and now commonly utilizes the refinement due to Lilly [14]. El-Hady *et al.* [15] applied the model to a transitional supersonic axisymmetric boundary layer with satisfactory results, while other applications have consisted of channel flows [16–18], a lid-driven cavity [19], and mixing layers [10].

Despite advances in computing capacity, large-eddy and direct simulations are still limited by resolution requirements of flows at high Reynolds number, especially near wall-bounded regions. Spectral and pseudo-spectral methods have successfully provided highly accurate results for simple geometries, but lack the flexibility which is required for treating more complex practical configurations. Although finite-difference and finite-volume techniques are considerably more versatile, low-order methods cannot satisfy the resolution demands of high-Reynolds number flows. Difference schemes with high spatial accuracy are therefore attractive for LES and DNS computations, and have been shown to be desirable for their ability to improve subgrid model performance and to reduce aliasing errors [20, 21]. Currently, most of these procedures are employed in conjunction with explicit time advancement algorithms. The focus of the work presented here is to evaluate the use of a time-implicit high-order compact finite-difference scheme for large-eddy simulations.

A major problem associated with the application of non-dissipative spatial discretizations to LES on general curvilinear stretched meshes, is the generation of high-frequency modes which

contaminate the solution and can ultimately result in numerical instability. To overcome this difficulty in the present approach, the solution variables are filtered by employing tenth-order Pade-type low-pass operators, which were previously developed and evaluated by Gaitonde *et al.* [22]. This compact differencing and filtering technique has proven to be highly accurate and robust for wave propagation [22], and for the simulation of vortical flows [23]. However, the impact of filtering on LES has not been assessed previously, and this constitutes one of the main objectives of the present investigation.

While explicit methods provide accurate temporal resolution for LES and DNS, the time step size is dictated by stability constraints of the algorithm rather than by the frequency content of the large-scale structures. This can be a severe constraint, particularly for low-Mach number and wall-bounded flows. In addition, the situation is exacerbated since computations must be carried out for extended periods of time in order to collect statistical information. The implicit technique may thus afford a desirable alternative by allowing larger time increments.

The present effort considers the application of a time-implicit high-order compact differencing and filtering scheme to compressible large-eddy simulations. The governing equations are summarized, including a description of the SGS stress models, and details of the numerical procedure are presented. Computations are performed for a series of classic validating flows, consisting of the decay of compressible isotropic turbulence, turbulent channel flow, and the subsonic flow past a circular cylinder. Large-eddy simulations and results employing no subgrid-stress model are compared for each case, along with experimental data and previous existing computations.

2. GOVERNING EQUATIONS

The governing equations are the unsteady three-dimensional compressible Favre filtered Navier–Stokes equations, written in non-dimensional variables and expressed notationally in the following conservative form:

$$\frac{\partial Q}{\partial t} + \frac{\partial}{\partial \xi}\left(F - \frac{1}{Re}F_{\mathrm{v}}\right) + \frac{\partial}{\partial \eta}\left(G - \frac{1}{Re}G_{\mathrm{v}}\right) + \frac{\partial}{\partial \zeta}\left(H - \frac{1}{Re}H_{\mathrm{v}}\right) + S = 0 \tag{1}$$

Here t is the time, ξ, η, ζ the computational co-ordinates, Q the vector of dependent variables, F, G, H the inviscid flux vectors, F_{v}, G_{v}, H_{v} the viscous flux vectors, and S a vector source term that is non-zero only for the computation of planar channel flows. The filtered form of an arbitrary variable f, is given by

$$\bar{f} = \int_{\mathscr{V}} \mathscr{G} f \, \mathrm{d}\mathscr{V} \tag{2}$$

where $\mathscr{G}$ is the grid filtering function and the integration is carried out over the entire flow domain. This allows f to be decomposed into its large-scale ($\bar{f}$) and subgrid-scale (f_{sg}) components

$$f = \bar{f} + f_{\mathrm{sg}} \tag{3}$$

It is then convenient for compressible flows to recast the large-scale component in terms of a Favre-averaged variable

$$\tilde{f} = \frac{\overline{\rho f}}{\bar{\rho}} \tag{4}$$

With this formulation, the vector of dependent variables is given as

$$Q = \frac{1}{J}\begin{bmatrix} \bar{\rho} \\ \bar{\rho}\tilde{u} \\ \bar{\rho}\tilde{v} \\ \bar{\rho}\tilde{w} \\ \bar{\rho}\tilde{E} \end{bmatrix} \tag{5}$$

and the vector fluxes by

$$F = \frac{1}{J}\begin{bmatrix} \bar{\rho}\tilde{U} \\ \bar{\rho}\tilde{u}\tilde{U} + \xi_x \bar{p} \\ \bar{\rho}\tilde{v}\tilde{U} + \xi_y \bar{p} \\ \bar{\rho}\tilde{w}\tilde{U} + \xi_z \bar{p} \\ \bar{\rho}\tilde{E}\tilde{U} + \xi_{x_i} u_i \bar{p} \end{bmatrix} \tag{6}$$

$$G = \frac{1}{J}\begin{bmatrix} \bar{\rho}\tilde{V} \\ \bar{\rho}\tilde{u}\tilde{V} + \eta_x \bar{p} \\ \bar{\rho}\tilde{v}\tilde{V} + \eta_y \bar{p} \\ \bar{\rho}\tilde{w}\tilde{V} + \eta_z \bar{p} \\ \bar{\rho}\tilde{E}\tilde{V} + \eta_{x_i} u_i \bar{p} \end{bmatrix} \tag{7}$$

$$H = \frac{1}{J}\begin{bmatrix} \bar{\rho}\tilde{W} \\ \bar{\rho}\tilde{u}\tilde{W} + \zeta_x \bar{p} \\ \bar{\rho}\tilde{v}\tilde{W} + \zeta_y \bar{p} \\ \bar{\rho}\tilde{w}\tilde{W} + \zeta_z \bar{p} \\ \bar{\rho}\tilde{E}\tilde{W} + \zeta_{x_i} u_i \bar{p} \end{bmatrix} \tag{8}$$

$$F_{\mathrm{v}} = \frac{1}{J}\begin{bmatrix} 0 \\ \xi_{x_i}(\tilde{\sigma}_{i1} + \tau_{i1}) \\ \xi_{x_i}(\tilde{\sigma}_{i2} + \tau_{i2}) \\ \xi_{x_i}(\tilde{\sigma}_{i3} + \tau_{i3}) \\ \xi_{x_i}[\tilde{u}_j(\tilde{\sigma}_{ij} + \tau_{ij}) - \tilde{q}_i - \mathcal{Q}_i] \end{bmatrix} \tag{9}$$

$$G_{\mathrm{v}} = \frac{1}{J}\begin{bmatrix} 0 \\ \eta_{x_i}(\tilde{\sigma}_{i1} + \tau_{i1}) \\ \eta_{x_i}(\tilde{\sigma}_{i2} + \tau_{i2}) \\ \eta_{x_i}(\tilde{\sigma}_{i3} + \tau_{i3}) \\ \eta_{x_i}[\tilde{u}_j(\tilde{\sigma}_{ij} + \tau_{ij}) - \tilde{q}_i - \mathcal{Q}_i] \end{bmatrix} \tag{10}$$

$$H_{\mathrm{v}} = \frac{1}{J}\begin{bmatrix} 0 \\ \zeta_{x_i}(\tilde{\sigma}_{i1} + \tau_{i1}) \\ \zeta_{x_i}(\tilde{\sigma}_{i2} + \tau_{i2}) \\ \zeta_{x_i}(\tilde{\sigma}_{i3} + \tau_{i3}) \\ \zeta_{x_i}[\tilde{u}_j(\tilde{\sigma}_{ij} + \tau_{ij}) - \tilde{q}_i - \mathcal{Q}_i] \end{bmatrix} \tag{11}$$

with the vector source term

$$S = \frac{1}{J}\begin{bmatrix} 0 \\ s_1 \\ s_2 \\ s_3 \\ s_i\tilde{u}_i \end{bmatrix} \tag{12}$$

where

$$\tilde{U} = \xi_t + \xi_{x_i}\tilde{u}_i \tag{13}$$

$$\tilde{V} = \eta_t + \eta_{x_i}\tilde{u}_i \tag{14}$$

$$\tilde{W} = \zeta_t + \zeta_{x_i}\tilde{u}_i \tag{15}$$

$$\tilde{E} = \frac{\tilde{T}}{(\gamma - 1)M_{\mathrm{r}}^2} + \frac{1}{2}(\tilde{u}^2 + \tilde{v}^2 + \tilde{w}^2) \tag{16}$$

In the preceding expressions, $\tilde{u}, \tilde{v}, \tilde{w}$ are the Cartesian velocity components, $\bar{\rho}$ the density, $\bar{p}$ the pressure, and $\tilde{T}$ the temperature. All length scales have been non-dimensionalized by a representative distance l_{r}, and dependent variables have been normalized by their reference values except for $\bar{p}$ which has been non-dimensionalized by $\rho_{\mathrm{r}}u_{\mathrm{r}}^2$. Components of the heat flux vector and stress tensor may be expressed as

$$\tilde{\sigma}_{ij} = \tilde{\mu}\left(\frac{\partial\xi_k}{\partial x_j}\frac{\partial\tilde{u}_i}{\partial\xi_k} + \frac{\partial\xi_k}{\partial x_i}\frac{\partial\tilde{u}_j}{\partial\xi_k} - \frac{2}{3}\delta_{ij}\frac{\partial\xi_l}{\partial x_k}\frac{\partial\tilde{u}_k}{\partial\xi_l}\right) \tag{17}$$

$$\tilde{q}_i = -\left[\frac{1}{(\gamma - 1)M_{\mathrm{r}}^2}\right]\left(\frac{\tilde{\mu}}{Pr}\right)\frac{\partial\xi_j}{\partial x_i}\frac{\partial\tilde{T}}{\partial\xi_j} \tag{18}$$

while the corresponding subgrid-scale stress and heat flux are provided by

$$\tau_{ij} = -Re\,\bar{\rho}(\widetilde{u_i u_j} - \tilde{u}_i \tilde{u}_j) \tag{19}$$

$$\mathscr{Q}_i = Re\,\bar{\rho}(\widetilde{u_i T} - \tilde{u}_i \tilde{T}) \tag{20}$$

For direct-numerical simulations, all variables may be replaced by their unfiltered forms and τ_{ij} and $\mathscr{Q}_i$ vanish, whereas for large-eddy computations, τ_{ij} and $\mathscr{Q}_i$ are obtained from the SGS model.

The Sutherland law for the molecular viscosity coefficient $\tilde{\mu}$ and the perfect gas relationship

$$\bar{p} = \frac{\bar{\rho}\tilde{T}}{\gamma M_r^2} \tag{21}$$

are also employed, as is Stokes' hypothesis for the bulk viscosity coefficient.

Complete definitions of the nomenclature appearing in the above and subsequent equations may be found in Reference [24].

2.1. Smagorinsky subgrid-stress model

The first subgrid stress model was developed for incompressible flows by Smagorinsky [1], based upon the assumption that the turbulent kinetic energy production of the small-scale structures is balanced by dissipation. The compressible version of the model in trace-free form is given as

$$\mu_t = ReC\Delta^2 \bar{\rho}\tilde{\mathscr{S}}_M \tag{22}$$

where

$$\tilde{\mathscr{S}}_M = (2\tilde{\mathscr{S}}_{ij}\tilde{\mathscr{S}}_{ij})^{1/2} \tag{23}$$

is the magnitude of the rate-of-strain tensor, and

$$\tilde{\mathscr{S}}_{ij} = \frac{1}{2}\left(\frac{\partial \xi_k}{\partial x_j}\frac{\partial \tilde{u}_i}{\partial \xi_k} + \frac{\partial \xi_k}{\partial x_i}\frac{\partial \tilde{u}_j}{\partial \xi_k}\right) \tag{24}$$

The eddy-viscosity length scale is taken as

$$\Delta = \left(\frac{1}{J}\right)^{1/3} \tag{25}$$

C is the eddy-viscosity model constant, and

$$\tau_{ij} - \frac{1}{3}\tau_{kk}\delta_{ij} = -2\mu_t\left(\tilde{\mathscr{S}}_{ij} - \frac{1}{3}\tilde{\mathscr{S}}_{kk}\delta_{ij}\right) \tag{26}$$

The isotropic part of the stress tensor, $\frac{1}{3}\tau_{kk}$, is commonly neglected in low Mach number flows and the model degenerates to the original Smagorinsky form. For compressible applications, this term is accounted for according to Yoshizawa [25] as

$$\tau_{kk} = 2C_I\Delta^2\bar{\rho}\tilde{\mathscr{S}}_M^2 \tag{27}$$

To complete closure of the model, the subgrid-scale heat flux vector is specified in terms of a constant turbulent Prandtl number as

$$\mathscr{Q}_i = -\left(\frac{\mu_t}{Pr_t}\right)\frac{\partial \xi_j}{\partial x_i}\frac{\partial \tilde{T}}{\partial \xi_j} \tag{28}$$

The original Smagorinsky constant was given as $C_S = \sqrt{C}$. In near-wall regions, C_S must be multiplied by the van Driest damping factor

$$1 - \exp\left(\frac{n^+}{A^+}\right) \tag{29}$$

for the eddy viscosity to attain a more correct limiting behaviour, where n^+ is the normal distance from the solid surface in law-of-the-wall co-ordinates, and A^+ is the van Driest constant.

2.2. Dynamic subgrid-stress model

A dynamic SGS model was first proposed by Germano *et al.* [12] for incompressible flows, and extended by Moin *et al.* [13] for compressible applications. Its general formulation is identical to that of Smagorinsky and Yoshizawa given by Equations (22)–(28). In this description, however, the model 'constants' C and C_I are computed as a function of time and space from the energy content of the resolved large-scale structures. This is accomplished by introducing a test filter function $\hat{\mathscr{G}}$, with a filter width that is wider than the computational mesh, where its application is represented as

$$\hat{f} = \int_{\mathscr{V}} \hat{\mathscr{G}} f \, \mathrm{d}\mathscr{V}. \tag{30}$$

Differences between the subtest-scale stress and the subgrid-scale stress are then used to obtain values for the model constants. Details of the derivation may be found in References [12–14] which result in

$$C\Delta^2 = \frac{\langle (\mathscr{L}_{ij} - \frac{1}{3}\mathscr{L}_{kk}\delta_{ij})\mathscr{M}_{ij}\rangle}{\langle \mathscr{M}_{ij}\mathscr{M}_{ij}\rangle} \tag{31}$$

where

$$\mathscr{L}_{ij} = \widehat{\bar{\rho}\tilde{u}_i\tilde{u}_j} - \frac{1}{\hat{\bar{\rho}}}\widehat{\bar{\rho}\tilde{u}_i}\,\widehat{\bar{\rho}\tilde{u}_j} \tag{32}$$

and

$$\mathscr{M}_{ij} = -2(\hat{\Delta}/\Delta)^2\hat{\bar{\rho}}\hat{\tilde{\mathscr{S}}}_M\left(\hat{\tilde{\mathscr{S}}}_{ij} - \tfrac{1}{3}\hat{\tilde{\mathscr{S}}}_{kk}\delta_{ij}\right) + 2\bar{\rho}\widehat{\tilde{\mathscr{S}}_M\left(\tilde{\mathscr{S}}_{ij} - \tfrac{1}{3}\tilde{\mathscr{S}}_{kk}\delta_{ij}\right)} \tag{33}$$

The normal stress constant is given by

$$C_I \Delta^2 = \frac{\langle \mathscr{L}_{kk} \rangle}{\langle 2(\hat{\Delta}/\Delta)^2 \hat{\bar{\rho}} \hat{\mathscr{S}}_M^2 - 2\widehat{\bar{\rho}\mathscr{S}_M^2} \rangle} \tag{34}$$

For the above expressions, the quantities enclosed by angled brackets ($\langle\,\rangle$) indicate that a spatial average is to be performed along directions in which a particular flow may be homogeneous. This is necessary to prevent certain quantities from vanishing, for example the denominator of Equation (34), which would then invalidate evaluation of the coefficients. In complex three-dimensional flows, more localized space and time averages must be employed. Recent attempts to perform such averages include the works of Piomelli and Liu [26], Meneveau *et al.* [27], and Wu and Squires [28]. When extended to the heat flux vector, the analysis also allows the turbulent Prandtl number to be determined as

$$Pr_t = C\Delta^2 \frac{\langle \mathscr{N}_i \mathscr{N}_i \rangle}{\langle -\mathscr{K}_i \mathscr{N}_i \rangle} \tag{35}$$

where

$$\mathscr{K}_i = \widehat{\bar{\rho}\tilde{u}_i \tilde{T}} - \frac{1}{\hat{\bar{\rho}}} \widehat{\bar{\rho}\tilde{u}_i} \widehat{\bar{\rho}\tilde{T}} \tag{36}$$

and

$$\mathscr{N}_i = (\hat{\Delta}/\Delta)^2 \hat{\bar{\rho}} \hat{\mathscr{S}}_M \frac{\partial \xi_j}{\partial x_i} \frac{\partial \hat{\tilde{T}}}{\partial \xi_j} - \widehat{\bar{\rho}\mathscr{S}_M \frac{\partial \xi_j}{\partial x_i} \frac{\partial \tilde{T}}{\partial \xi_j}} \tag{37}$$

The only adjustable parameter inherent in the model is the ratio of the test-filter width to the grid-filter width, $\hat{\Delta}/\Delta$. For all of the computations presented here, this ratio is taken as 2.0, which is consistent with the formulation of Germano *et al.* [12]. Besides the added complexity of the model formulation and associated numerical implementation, a major disadvantage of the model are the additional computational resources required to evaluate the model coefficients. In the computational examples that follow, the coefficients C, C_I, and Pr_t were numerically restricted to always be non-negative. Details of the test filter application are described in the following section.

3. NUMERICAL METHOD

Time-accurate solutions to Equation (1) were obtained numerically by the implicit approximately factored finite-difference algorithm of Beam and Warming [29] employing Newton-like subiterations [30], which has evolved as an efficient tool for generating solutions to a wide variety of complex fluid flow problems, and may be represented notationally as follows:

$$\left[I + \left(\frac{2\Delta t}{3} \right) \delta_{\xi 2} \left(\frac{\partial F^p}{\partial Q} - \frac{1}{Re} \frac{\partial F_v^p}{\partial Q} \right) \right]$$
$$\times \left[I + \left(\frac{2\Delta t}{3} \right) \delta_{\eta 2} \left(\frac{\partial G^p}{\partial Q} - \frac{1}{Re} \frac{\partial G_v^p}{\partial Q} \right) \right]$$

$$\times \left[I + \left(\frac{2\Delta t}{3} \right) \delta_{\zeta 2} \left(\frac{\partial H^p}{\partial Q} - \frac{1}{Re} \frac{\partial H_v^p}{\partial Q} \right) \right] \Delta Q$$

$$= - \left(\frac{2\Delta t}{3} \right) \left[\left(\frac{1}{2\Delta t} \right) (3Q^p - 4Q^n + Q^{n-1}) \right.$$

$$\left. + \delta_{\xi 6} \left(F^p - \frac{1}{Re} F_v^p \right) + \delta_{\eta 6} \left(G^p - \frac{1}{Re} G_v^p \right) + \delta_{\zeta 6} \left(H^p - \frac{1}{Re} H_v^p \right) \right] \tag{38}$$

In this expression, which was employed to advance the solution in time, Q^{p+1} is the $p+1$ approximation to Q at the $n+1$ time level Q^{n+1}, and $\Delta Q = Q^{p+1} - Q^p$. For $p = 1$, $Q^p = Q^n$. Second-order accurate backward-implicit time differencing has been used to represent temporal derivatives, and spatial difference operators appearing in the explicit portion of the algorithm (right-hand side) were evaluated by a sixth-order compact difference scheme. For convenience, the source term S has been treated explicitly, which does not adversely impact stability due to the use of subiteration.

The implicit segment of the algorithm incorporated second-order accurate centered differencing for all spatial derivatives, and utilized nonlinear artificial dissipation [31] to augment stability. Efficiency was enhanced by solving this implicit portion of the factorized equations in diagonalized form [32]. Temporal accuracy, which can be degraded by use of the diagonal form, is maintained by utilizing subiterations within a time step. This technique has been commonly invoked in order to reduce errors due to factorization, linearization, and explicit application of boundary conditions. It is useful for achieving temporal accuracy on overset zonal mesh systems, and for a domain decomposition implementation on parallel computing platforms. Any deterioration of the solution caused by the use of artificial dissipation and by lower-order spatial resolution of implicit operators is also reduced by the procedure. Three subiterations per time step have been applied for the computations presented here, which have been show to be suitable for previous computations [33].

The compact difference scheme employed on the right-hand side of Equation (38) is based upon the pentadiagonal system of Lele [34], and is capable of attaining spectral-like resolution. This is achieved through the use of a centered implicit difference operator with a compact stencil, thereby reducing the associated discretization error. The sixth-order tridiagonal subset of Lele's system is illustrated here in one spatial dimension as

$$\alpha \left(\frac{\partial f}{\partial \xi} \right)_{i-1} + \left(\frac{\partial f}{\partial \xi} \right)_i + \alpha \left(\frac{\partial f}{\partial \xi} \right)_{i+1} = a \left(\frac{f_{i+1} - f_{i-1}}{2} \right) + b \left(\frac{f_{i+2} - f_{i-2}}{4} \right) \tag{39}$$

with

$$\alpha = 1/3, \quad a = 14/9, \quad b = 1/9 \tag{40}$$

The scheme has been adapted by Visbal and Gaitonde [35] as an implicit iterative time-marching technique, applicable for unsteady vortical flows. It is used in conjunction with a 10th-order non-dispersive spatial filter developed by Gaitonde *et al.* [22], which has been shown to be superior to the use of explicitly added artificial dissipation for maintaining both stability and accuracy on stretched curvilinear meshes [23].

In the computational examples that follow, the test filter incorporated for the dynamic subgrid stress model was formulated as a one-dimensional seven-point explicit centered stencil in each co-ordinate direction. Coefficients of the stencil were obtained by performing a least squares curve fit of the filter transfer function to that of a sharp-cutoff filter, where the filter width was approximately twice that of the 10th-order spatial filter which was employed for solution of the flow equations. Spatial derivatives which must be evaluated for the computation of $\tilde{\mathscr{G}}_M$ were approximated by fourth-order explicit stencils, which were shown to be adequate in preliminary studies.

The aforementioned features of the numerical algorithm are embodied in an existing fully-vectorized time-accurate three-dimensional computer code FDL3DI [35], which has proven to be reliable for steady and unsteady fluid flow problems, including the simulation of flows over delta wings with leading-edge vortices [30, 36–39], vortex breakdown [36–39], and the direct-numerical simulation of transitional wall jets [39] and synthetic jet actuators [40]. While attention of this investigation is concentrated on the implicit time-advancement method, FDL3DI also provides the optional fourth-order Runge–Kutta explicit integration scheme (RK4), implemented in low-storage form [41].

4. RESULTS

Results of specific validating computations are described below, a more comprehensive presentation of which appears in Reference [24]. Flow conditions and associated parameters for each of the cases considered are found in Table I. In all situations where periodic boundaries occur, these are implemented numerically by employing an overlap of five grid points in the mesh across the domain edges. With this procedure, it is unnecessary to revert to either a one-sided difference stencil or reduced spatial accuracy at domain boundaries. A minimal computational overhead is incurred, but sixth-order central differencing and the overall integrity of the scheme is maintained.

For the computations that follow, we use the term ‘no model’ to refer to solutions in which no subgrid-stress model was explicitly employed. In some case, the grids utilized for these no-model results may have been sufficiently fine to resolve all the important physical scales, so that they may be considered direct numerical simulations (DNS). Otherwise, such solutions are sometimes designated monotonically integrated large-eddy simulation (MILES [24, 42]), whereby nonlinear high-frequency filters built into numerical algorithms provide implicit SGS models [43]. In the present applications, this was engendered by the 10th-order non-dispersive spatial filter.

Table I. Flow conditions and parameters.

Case	l_r	u_r	M_r	Re	C_S	C_I	A^+
Decay	(Domain size)/2π	Initial mean sound speed	1.0	536.9	0.0920	0.0066	
Channel	Channel height	Mean centreline velocity	0.1	7700.0	0.0920	0.0000	25.0
Cylinder	Cylinder diameter	Freestream velocity	0.1	3900.0	0.0650	0.0000	25.0

4.1. Compressible decaying isotropic turbulence

One of the simplest compressible turbulent flowfields is that of decaying isotropic turbulence. This flow has been used to investigate compressible formulations of SGS models for large-eddy simulations by Moin [13] and Spyropoulos and Blaisdell [44] among others. For the present computations, the domain size is $(2\pi \times 2\pi \times 2\pi)$ in (x, y, z), which is described by a mesh of uniformly distributed grid points. Periodic conditions are enforced at all edges of the domain boundary. The flowfield is initialized by specifying the three-dimensional spectra for velocity, density and temperature as described in Reference [44]. Although improved initial conditions which do not generate acoustic waves are available [45], the current set was chosen because previous DNS and LES computations [44] are available for comparison.

The isotropic turbulence simulations considered here correspond to Case 6 of Reference [44]. A reference length l_r is chosen so that the domain size has a length of 2π on each side, as noted above. The length scale of the turbulence is then defined by specifying the form of the initial three-dimensional spectra as

$$E_{3D} \propto k^4 \exp[-2(k/k_p)^2] \tag{41}$$

where k is the magnitude of the wave number vector, and the wave number at the peak in the spectrum k_p is set to 4. Root-mean-square (RMS) levels of the velocity, density, and temperature are established by adjusting the proportionality constant in the spectra. The RMS level of the velocity is specified so that the initial turbulent Mach number $M_t = 0.4$, where M_t is defined as the ratio of the RMS magnitude of the fluctuating velocity to the mean speed of sound. The reference velocity u_r is chosen to be the initial mean sound speed, so that $M_r = 1$. In addition to the turbulent Mach number, the velocity field is parameterized by the fraction of energy in the dilatational part of the velocity, χ (see Reference [44]). In the current simulations, initial values are given by

$$\chi = 0.2 \tag{42}$$

$$\rho'^2_{rms}/\langle\rho\rangle^2 = 0.032 \tag{43}$$

$$T'^2_{rms}/\langle T\rangle^2 = 0.005 \tag{44}$$

The Reynolds number Re is determined as 536.9, which corresponds to a turbulent Reynolds number of 2157.0 (see Reference [44]).

A summary of current and previous simulations of compressible decaying isotropic turbulence appears in Table II. It should be noted that the grid sizes stated for the present computations do not include the five-point overlap at domain boundaries.

Evolution of the turbulent kinetic energy is shown in Figure 1, where

$$K = \langle\rho(u'^2 + v'^2 + w'^2)\rangle. \tag{45}$$

In the figure, time has been scaled by the initial eddy turnover time t_{et}, which is defined as the ratio of K to the dissipation rate. An approximate time step of $\Delta t/t_{et} = 0.0004$ was employed for all simulations. Along with the present time-implicit simulations, one result was also obtained using the explicit RK4 scheme. Computations on the finest grid using no

Table II. Summary of decaying isotropic turbulence simulations.

Reference	SGS model	Numerical method	Grid size
Spyropoulos and Blaisdell [44]	None	Spectral	$(128 \times 128 \times 128)$
Present	None	Finite difference	$(128 \times 128 \times 128)$
Present	Smagorinsky	Finite difference	$(64 \times 64 \times 64)$
Present	Dynamic	Finite difference	$(64 \times 64 \times 64)$
Present	Smagorinsky	Finite difference	$(32 \times 32 \times 32)$
Present	Dynamic	Finite difference	$(32 \times 32 \times 32)$
Spyropoulos and Blaisdell [44]	Dynamic	Spectral	$(32 \times 32 \times 32)$

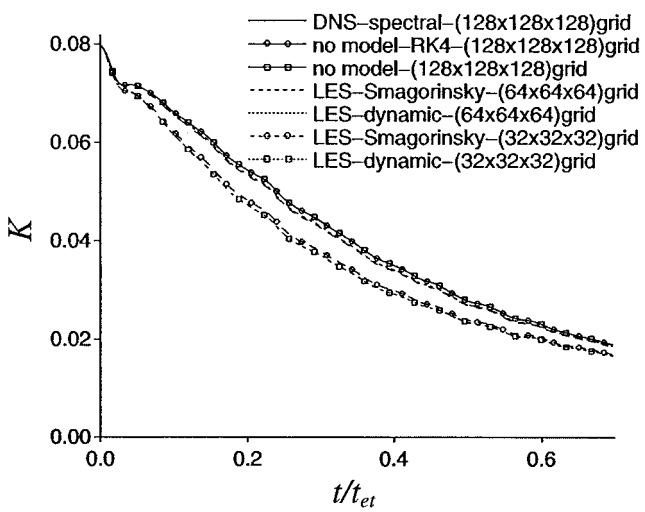

Figure 1. Time history of decaying turbulence kinetic energy.

subgrid-stress model are indistinguishable from the highly resolved spectral computation of Spyropoulos and Blaisdell [44], providing validation of the current numerical approach and computer code. Comparison of the time-implicit computations with those employing the RK4 scheme also indicates that second-order temporal accuracy is sufficient to attain DNS resolution for this case. Also seen in Figure 1 are four LES solutions on two separate grid systems. Both LES computations on the $(64 \times 64 \times 64)$ grid give virtually identical results, implying that there is little sensitivity to the form of the SGS model. Although the LES calculations should be compared to filtered DNS solutions, for this low Reynolds number example, the application of a sharp cutoff filter resulted in values of K that were only slightly different than those of their unfiltered counterparts. LES results on the $(64 \times 64 \times 64)$ grid are observed to lie slightly below those of the DNS solutions. Examination of the energy spectrum will reveal that this is due to a reduction of the turbulent kinetic energy in the higher resolved wave numbers. Computations on the $(32 \times 32 \times 32)$ grid lie significantly below those of the DNS, indicating that this mesh is probably too coarse to be employed for the finite-difference calculations.

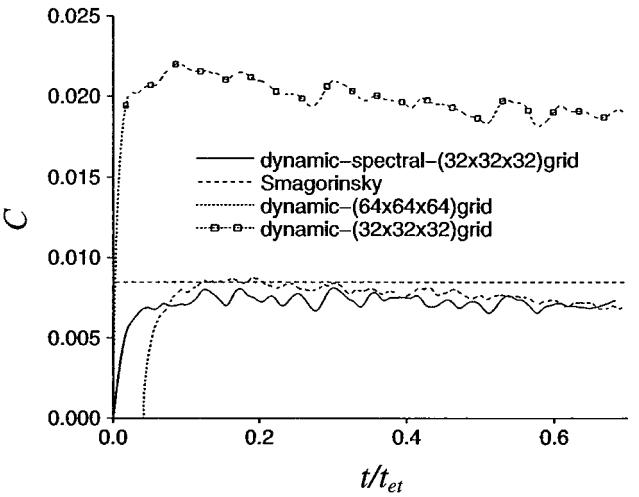

Figure 2. Time history of decaying turbulence eddy viscosity model constant.

The time-varying coefficient C from the present and spectral dynamic model simulations appears in Figure 2. These are compared with the constant value of 0.092 assumed in the Smagorinsky model. Values of C obtained from the current computation on the $(32 \times 32 \times 32)$ grid are considerably greater than those of the spectral result, again illustrating the excessive coarseness of this mesh. As the grid is refined, the level of C from the current solution approaches that of the spectral result. It is pointed out that as the computational mesh is refined, eventually all important length scales will be resolved without the need for subgrid-stress modelling. Thus the coefficient C will tend toward zero and a DNS solution will be recovered. This feature of the dynamic subgrid-stress model is consistent with the results of Figure 2. Corresponding evolutions of the turbulent Prandtl number can be found in Reference [24].

Displayed in Figure 3 is the instantaneous three-dimensional energy spectrum for the current solutions at $t/t_{\mathrm{et}} = 0.2985$. No significant differences between the two LES results are indicated, confirming again that the form of the subgrid stress model is not an important factor for this simulation. For the $(64 \times 64 \times 64)$ grid, both LES computations compare well with the more resolved no-model (DNS) simulation over most of the wave number range. The coarser $(32 \times 32 \times 32)$-grid solutions have less energy in the higher wave numbers, which is responsible for the reduced turbulent kinetic energy of the LES in Figure 1.

Recent computations by Visbal and Rizzetta [33] have directly compared the efficiency of the present technique to that of standard low-order methods for this same problem. It was shown that a second-order scheme requires a grid between two to four times finer than that of the compact/filtering approach in order to achieve the same level of accuracy. This translates to an increase in the total number of grid points by a factor of 8–64. In terms of CPU time required per grid point per time step, the high-order scheme exceeds that of a second-order method by a factor of 2.0. Therefore, a significant net gain in efficiency is achieved with the high-fidelity formulation.

A more comprehensive investigation of compressible decaying isotropic turbulence is beyond the scope of the present work. Further simulations would be required, however, to

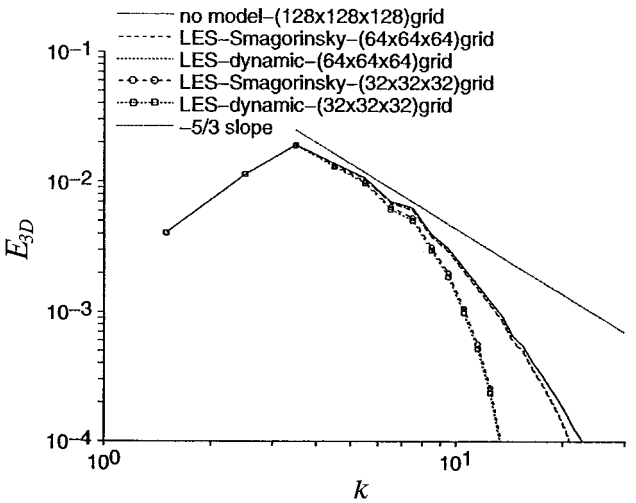

Figure 3. Instantaneous decaying turbulence three-dimensional energy spectra at $t/t_{\mathrm{et}} = 0.2985$.

address issues concerning grid size and filtering operations. Examples at higher Reynolds numbers may provide a more severe test of the capabilities of the numerical method, and such cases are available for comparison [44].

4.2. Turbulent channel flow

A number of large-eddy simulations for low-Reynolds number channel flows have been performed, some of which are documented in References [3–7, 16–18], and [49, 50]. For the situation considered here, x, y, z are taken as the streamwise, wall normal, and spanwise directions respectively, where the origin of the co-ordinate system is located at the upstream lower inboard boundary of the channel flowfield. The Reynolds number $Re = 7700$, corresponds to the oil channel experiment of Kreplin and Eckelmann [46] which may be used for comparison of fluctuating velocity components, along with the mean profiles of Eckelmann [47].

The non-dimensional computational domain size is $(2\pi \times 1 \times \pi)$ in (x, y, z), which is discretized by a baseline grid of $(65 \times 61 \times 65)$ points. Mesh spacing is constant in the x and z directions, and geometrically stretched in y from the walls, where $\Delta y = 0.001$. This corresponds to $\Delta y^+ = 0.389$, $\Delta x^+ = 40.70$ and $\Delta z^+ = 20.35$.

Periodic boundary conditions are applied for all variables in the streamwise and spanwise directions. At the channel walls, the no slip condition is satisfied, along with an isothermal surface and a vanishing normal pressure gradient, which are enforced with fourth-order spatial accuracy. Because of the periodic streamwise boundary condition, the flow cannot sustain a streamwise pressure gradient. It is therefore necessary to introduce an artificial source term as a driving mechanism to mimic an imposed constant pressure gradient, thereby maintaining a fixed mass-flow rate. The source term appearing in Equation (1) is generated by considering the steady two-dimensional limiting form of the ξ-momentum equation and integrating over

the channel height, $0 \leqslant \eta \leqslant N$, resulting in

$$s_1 = \left[Re \int_0^N \left(\frac{1}{J} \right) \mathrm{d}\eta \right]^{-1} \left\{ \left[\left(\frac{\tilde{\mu} \eta_y^2}{J} \right) \frac{\partial \tilde{u}}{\partial \eta} \right] \Bigg|_{\eta = N} - \left[\left(\frac{\tilde{\mu} \eta_y^2}{J} \right) \frac{\partial \tilde{u}}{\partial \eta} \right] \Bigg|_{\eta = 0} \right\} \tag{46}$$

and

$$s_2 = s_3 = 0 \tag{47}$$

Equation (46) is evaluated instantaneously and implemented numerically by averaging surface values over the lower and upper channel walls, which are located at $\eta = 0$ and N, respectively.

Uniform properties of $\bar{\rho}$, $\bar{p}$, and $\tilde{T}$ were used to initialize the flowfield along with $\tilde{v} = \tilde{w} = 0$, and $\tilde{u}$ was distributed according to the empirical polynomial approximation of Pai [48]. Random perturbations with a maximum amplitude of ± 0.05 were then superimposed upon $\tilde{u}, \tilde{v}, \tilde{w}$, and the flowfield was allowed to evolve to a fully turbulent state. A time increment was specified as $\Delta t = 0.001$, and temporal data was collected for a minimum of 40 000 steps for each case considered. Mean and RMS values were averaged over x–z planes to obtain the one-dimensional profiles considered here, as is common for domains with periodic boundaries. Large-eddy simulations employing the Smagorinsky subgrid stress model were carried out with the values $C_S = 0.092$ and $A^+ = 25.0$, which typically have been used in previous computations. Since the flow is essentially incompressible, the isotropic portion of the subgrid-scale stress tensor has been neglected, and a constant Prandtl number of 0.9 was assigned.

Time-mean streamwise velocity profiles for the outer channel region appear in Figure 4, along with the experimental measurements of Eckelmann [47] at two different Reynolds numbers. Only minor variations between the respective computations are apparent. It should be noted, however, that because the velocity is normalized by the centreline value, the profiles collapse to a similarity form. In each case, there is actually a slight overshoot of the centreline velocity, which for the no-model solution is approximately 7.5%. This is incurred due to the

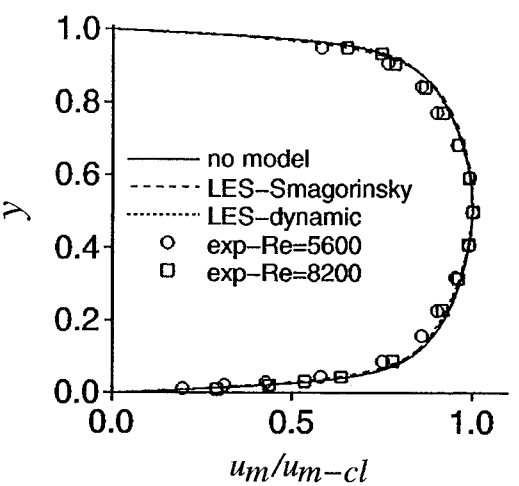

Figure 4. Planar averaged channel mean streamwise velocity profiles in outer flow region.

Table III. Channel flow friction velocity.

Reference	SGS model	Grid size	$u_{\tau-m}/u_{cl-m}$
Present	None	$(35 \times 61 \times 35)$	0.0415
Present	None	$(65 \times 61 \times 65)$	0.0535
Present	None	$(95 \times 91 \times 95)$	0.0547
Present	Smagorinsky	$(65 \times 61 \times 65)$	0.0512
Present	Dynamic	$(65 \times 61 \times 65)$	0.0515
Kim *et al.* [49]	None	$(192 \times 129 \times 160)$	0.0553
Okong'o and Knight [50]	Smagorinsky	$(65 \times 65 \times 65)$	0.0514
Kreplin and Eckelmann [46]	Experiment		0.0505

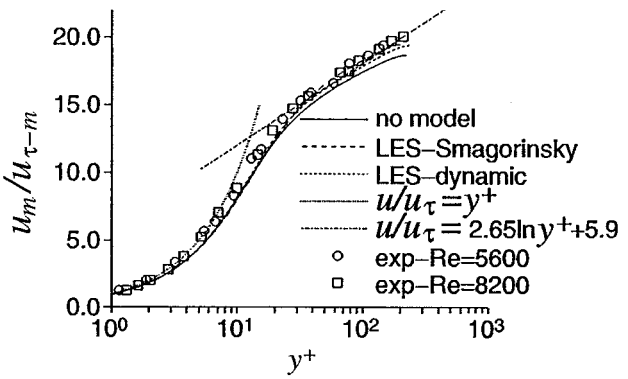

Figure 5. Planar averaged channel mean streamwise velocity profiles in near wall region.

non-dimensionalization by u_τ, which is not known *a priori*. Although the channel mass flow is established by the initial conditions of the computation, the velocity profile responds to the source term (Equation (46)) which also evolves as part of the solution. Thus, the variation in mean centreline velocity may be interpreted as the computed results corresponding to the somewhat higher Reynolds number $Re = 8300$.

In addition to computations performed on the baseline grid, no-model calculations were also carried out on grids with dimensions $(95 \times 91 \times 95)$ and $(35 \times 61 \times 35)$. The resulting time-mean friction velocity from all computations are listed in Table III, along with those of Kim *et al.* [49], Okong'o and Knight [50], and the experimental data of Kreplin and Eckelmann [46]. The computation of Kim *et al.* [49] at $Re = 6600$ affords a highly resolved DNS spectral solution. Present LES values compare favourably with the experiment, and with the recent computation of Okong'o and Knight [50] which was performed on a similar grid. Apart from the coarse-grid solution, all of the no-model results are higher than those of LES computations.

Profiles of the mean streamwise velocity in the near-wall region, normalized by the friction velocity and plotted as a function of the law-of-the-wall co-ordinate y^+, are displayed in Figure 5. Also found in the figure are the data of Eckelmann [47], the linear profile, and the logarithmic correlation which was compared to experimental values [47]. The LES profiles are virtually identical, and all results compare well with the data.

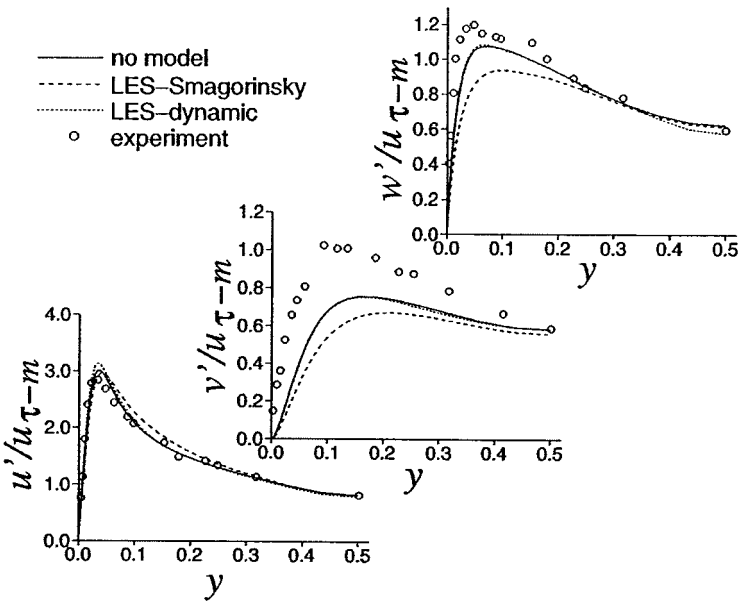

Figure 6. Planar averaged channel fluctuating velocity profiles in outer flow region.

For results presented in Figures 6, 7, and 9, velocity components denoted by u', v', w' are meant to indicate RMS values. Shown in Figure 6 are fluctuating velocity profiles in the outer portion of the channel. It is evident that the dynamic model LES and no-model solutions are virtually identical. All streamwise velocity (u') profiles compare well with the Kreplin and Eckelmann [46] experiment. The spanwise velocity (w') comparison is reasonable, but the normal velocity (v') is not well predicted. Generally, the Smagorinsky model LES solution compares less favourably with the data due to excessive dissipation. Corresponding near-wall fluctuating velocity profiles are presented in Figure 7 as a function of the law-of-the-wall co-ordinate y^+. The behaviour here is identical to the outer profiles in that the dynamic model LES and no-model solutions are quite similar, the streamwise velocity (u') component is well predicted in each case, and the Smagorinsky model LES solution compares less favourably with the experiment.

A grid resolution study of the no-model case was performed for the channel flowfield. The no-model case was selected for this investigation because the fine-scale structures, which are modelled in the LES computations, should be most sensitive to grid refinement. As mentioned previously, solutions for this case were obtained on coarse, baseline, and fine computational meshes. The mean streamwise and fluctuating velocity components resulting from this study are seen in Figures 8 and 9, respectively, where the DNS of Kim *et al.* [49] has been provided for comparison. It is noted in Figure 9 that the profiles of Kim *et al.* [49] have peaks in the near-wall region which are not as sharp as those of the present results. This is consistent with the lower Reynolds number employed in that simulation. Although it is apparent from the figures that the coarse-grid result is not resolved, a consistent trend with grid refinement is observed. Moreover, results on the baseline and finest grids are in close agreement, indicating that fine-scale structures, particularly on the fine grid, are adequately

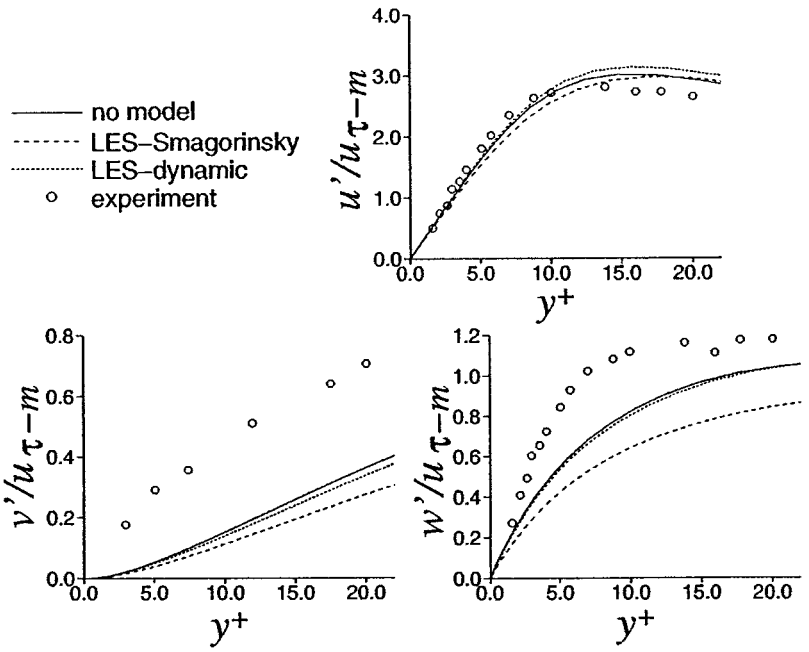

Figure 7. Planar averaged channel fluctuating velocity profiles in near wall region.

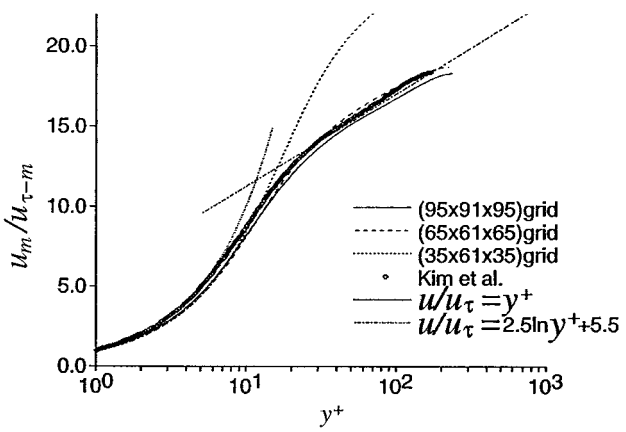

Figure 8. Effect of grid resolution on planar averaged channel mean streamwise velocity profiles in near wall region for no-model case.

defined. This demonstrates that mesh spacings of the baseline grid given in wall units on page 20, afford reasonable resolution. Corresponding near-wall fluctuating velocity components may be found in Reference [24], where a similar trend is indicated.

A representation of the fine-grid no-model flowfield is displayed in Figure 10 in terms of instantaneous contours of the z-component of vorticity at the channel midspan ($z = \pi/2$), and

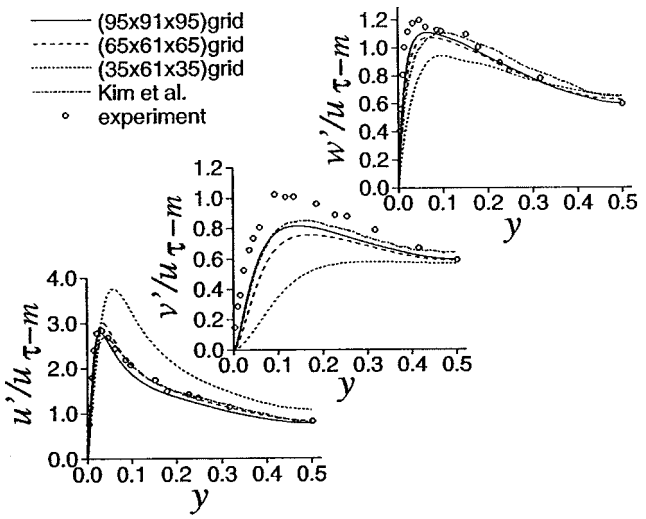

Figure 9. Effect of grid resolution on planar averaged channel fluctuating velocity profiles in outer flow region for no-model case.

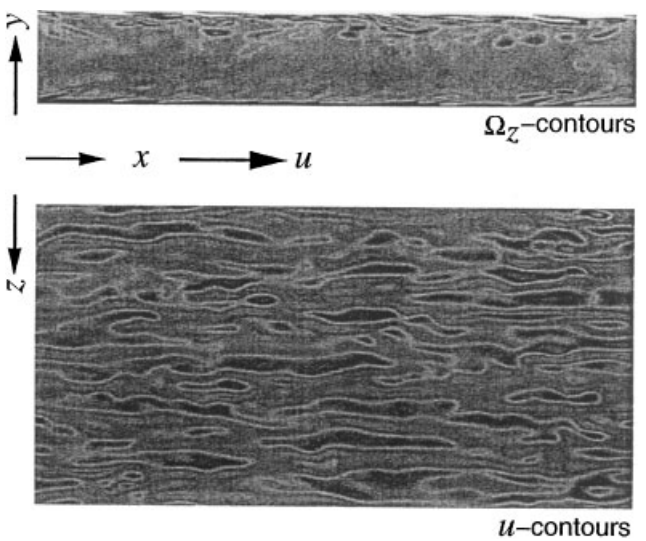

Figure 10. Instantaneous channel Ω_z contours at $z = \pi/2$ and velocity contours at $y = 0.0328$ for no-model case.

the streamwise velocity on an x–z plane in the near-wall flow at $y = 0.0328$ ($y^+ = 12.75$). The vorticity contours clearly illustrate hairpin-like structures in the near-wall region, while the pattern seen in the velocity contours is characteristic of low-speed streaks, both of which typify wall-bounded turbulent flows.

Instantaneous planar averaged eddy-viscosity profiles appear in Reference [24]. While the maximum values of those profiles was quite small ($\mu_t < 0.3$), the time-mean eddy viscosity

could be substantially larger. The small instantaneous values of μ_t, along with the grid resolution study, indicate that most of the turbulent energy for this flow is contained in the resolved structures. A similar conclusion was drawn by Okong'o and Knight [50].

4.3. Flow past a circular cylinder

Large-eddy simulations for the flow past a circular cylinder at a Reynolds number of $Re = 3900$ have been performed by Beaudan and Moin [51], Mittal and Moin [52], and Kravchenko and Moin [53]. Similar computations at a Reynolds number of $Re = 5600$ have also been carried out by Jordan and Ragab [54]. This situation represents a test for numerical methods which are capable of simulating regions with geometric curvature. Particle imaging velocimetry [51] and hot-wire experimental data [55] are available for comparison. In previous LES computations, it was found that the Smagorinsky SGS model did not provide a correct description of the flowfield in laminar regions where large gradients were present [51].

Current simulations were carried out on computational grids that consisted of $(199 \times 197 \times 53)$ points in the radial, circumferential, and spanwise directions, respectively. A Cartesian co-ordinate system was established with an origin coincident with the cylinder longitudinal axis, where (x, y, z) were oriented streamwise, vertical, and spanwise. Grid points were clustered near the cylinder surface, with a minimum normal spacing of 0.001, and non-uniformly stretched to an outer domain boundary that was situated 100 cylinder diameters from the origin. A concentration of circumferential grid lines near the wake centreline facilitated resolution of the experimentally measured region. Table IV provides a comparison of the mesh parameters for the present calculations with those of Beaudan and Moin [51] and Kravchenko and Moin [53]. Both of the prior computations employed numerical methods which provided spectral resolution in the spanwise direction. It should also be noted that Kravchenko and Moin utilized a high-order spline technique, implemented on a system of four patched grid networks and having an equivalent single mesh size of $(205 \times 185 \times 48)$ [53]. Unless explicitly stated otherwise, results of the present computations will correspond to designations B1, B2, and B3 of Table IV.

Along the upstream portion of the outer boundary, steady freestream conditions were prescribed for all dependent variables, which is consistent with previous numerical simulations [51, 53]. Downstream, the pressure was specified as freestream, and streamwise (x) gradients of other variables were forced to vanish. The no slip condition was invoked on the cylinder

Table IV. Summary of cylinder flow simulations.

Reference	Key	SGS model	Spanwise extent	Grid size
Present	A	None	π	$(199 \times 197 \times 53)$
Present	B1	None	$\pi/2$	$(199 \times 197 \times 53)$
Present	B2	Smagorinsky	$\pi/2$	$(199 \times 197 \times 53)$
Present	B3	Dynamic	$\pi/2$	$(199 \times 197 \times 53)$
Beaudan and Moin [51]	B-M1	None	π	$(144 \times 136 \times 48)$
Beaudan and Moin [51]	B-M2	Smagorinsky	π	$(144 \times 136 \times 48)$
Beaudan and Moin [51]	B-M3	Dynamic	π	$(144 \times 136 \times 48)$
Kravchenko and Moin [53]	K-M	Dynamic	π	1,333,472

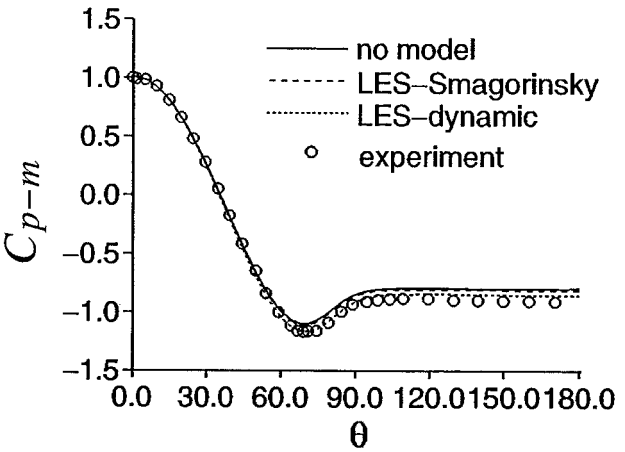

Figure 11. Spanwise averaged cylinder mean surface pressure distributions.

surface, together with fourth-order accurate approximations for an adiabatic wall and zero normal pressure gradient. At the spanwise boundaries, periodicity was applied.

The flowfield for a no-model computation was initialized from a preliminary two-dimensional unsteady result, and a solution was evolved sufficiently long in time to arrive at a time-asymptotic state. Temporal data was then collected for 20 000 time steps, corresponding to more than eight cycles of the fundamental Strouhal frequency. LES computations were initiated from the no-model flowfield, and allowed to develop for 4000 time steps before temporal information was recorded. The time step size in all computations was $\Delta t = 0.002$. Mean, RMS, and spectral information was averaged in the spanwise direction to arrive at the results presented below.

Computed mean surface pressure distributions are presented in Figure 11, along with experimental data [53]. Agreement between the simulations and the measurements is reasonable for all calculations, particularly in the upstream region. The dynamic model LES result lies closer to the experimental data on the aft cylinder surface. Distributions of the mean wake centreline velocity are seen in Figure 12. Two alternate sets of measurements [53] are provided for comparison. Here again, the dynamic model LES solution more closely resembles the experimental data.

In order to investigate the effect of spanwise grid resolution, two computational domains were considered which extended over distances of both π and $\pi/2$ in the z direction (see Table IV). Because periodic conditions are enforced in the spanwise direction, the span must be sufficiently long such that large-scale structures are not artificially forced to become two-dimensional. It has been established by Kravchenko and Moin [53] that a spanwise extent of $\pi/2$ satisfies this constraint. By maintaining a fixed number of mesh points, grid resolution could be examined with a minimal expenditure of computational resources by varying the span. Mean surface pressure results for the no-model case on each grid system appear in Figure 13. The no-model computations were again used for this investigation as they would be most sensitive to variations in mesh spacing. Subgrid-scale modelling in LES calculations should be able to tolerate a greater lack of resolution. The figure indicates, that while differences between

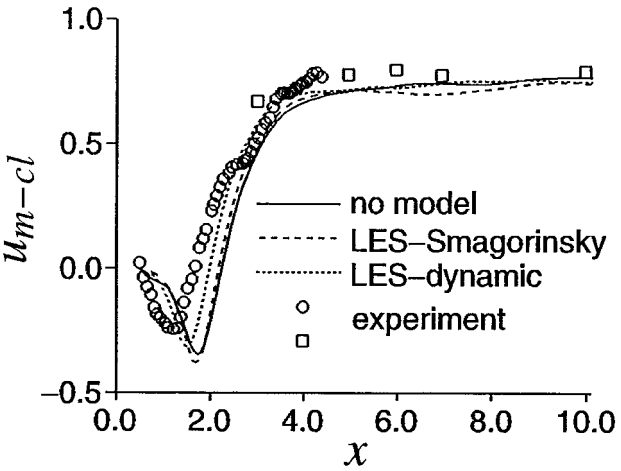

Figure 12. Spanwise averaged cylinder mean wake centreline streamwise velocity distributions.

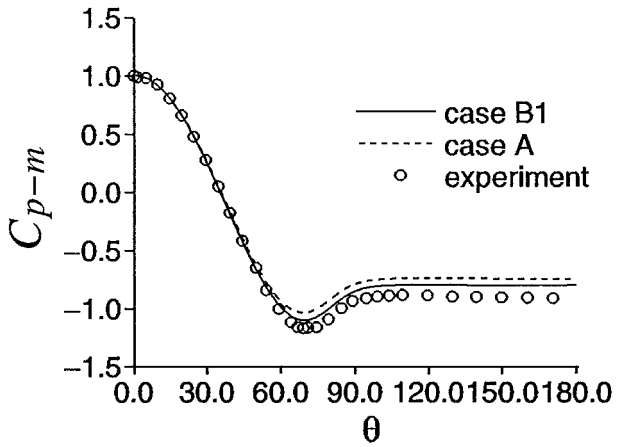

Figure 13. Effect of spanwise grid resolution on spanwise averaged cylinder mean surface pressure distribution for no-model case.

the two solutions are not large, the fine-grid result compares better to the experimental data. This is an indication that the no-model results for this case are under-resolved.

A number of results from the present cylinder flow computations are summarized in Table V, along with those from previous calculations and experimental data. Apart from the location of the mean primary separation point θ_{S-m}, the dynamic model LES solution (B3) compares more favourably with measured values than the no-model (A, B1) or Smagorinsky (B2) results.

Found in Figure 14 are vertical distributions of the mean streamwise velocity component. In general, the dynamic model LES solution affords the best comparison with experimental data. Corresponding distributions of the mean vertical velocity component are illustrated in

Table V. Cylinder flow results.

Key	C_{d-m}	C_{pB-m}	St	θ_{S-m}	L_{R-m}	$u_{\min-m}$
A	0.91	−0.74	0.210	86.7	2.01	−0.34
B1	0.94	−0.79	0.204	87.3	1.74	−0.34
B2	0.94	−0.81	0.211	87.4	1.67	−0.38
B3	0.97	−0.85	0.213	88.2	1.48	−0.31
B-M1	0.96	−0.89	0.216	85.3	1.56	−0.33
B-M2	0.92	−0.81	0.209	84.8	1.74	−0.33
B-M3	1.00	−0.95	0.203	85.8	1.36	−0.32
K-M	1.04	−0.94	0.210	88.0	1.35	−0.37
Exp. [53]	0.99±0.05	−0.88±0.05	0.215±0.005	86.0±2.0	1.40±0.10	−0.24±0.10

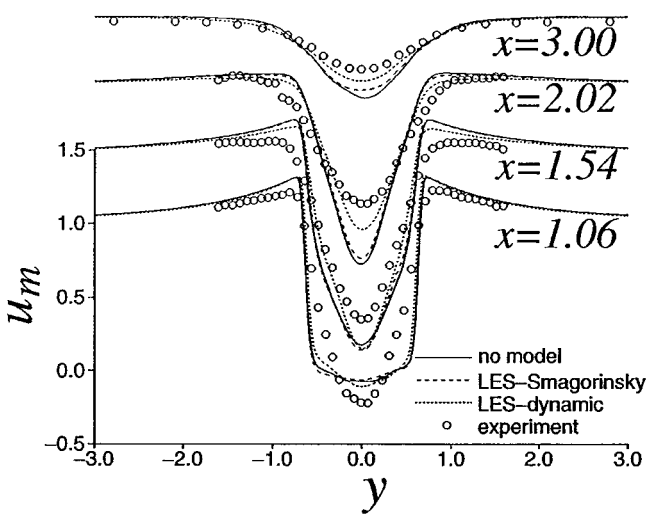

Figure 14. Spanwise averaged cylinder mean streamwise velocity distributions in near wake.

Figure 15. Because the magnitude of this component is small, only slight differences between the respective solutions are evident, except at $x = 1.54$.

Fluctuating velocity component distributions are presented in Figures 16–18, where once again RMS values are denoted by u', v'. For u'^2, the dynamic model LES results appear to agree better with the experiment in the near wake (Figure 16). This trend is also generally reflected in the vertical velocity fluctuation v'^2 seen in Figure 17. There does not appear to be a clear preferred performance trend for any of the solutions at all streamwise stations in terms of the Reynolds shear stress distributions shown in Figure 18.

One-dimensional velocity frequency spectra on the wake centreline ($y = 0$) at several streamwise stations are provided in Figure 19. The frequency (ω) has been normalized by the fundamental Strouhal shedding frequency in order to compare with experimental data [55]. Similarly, magnitudes of the velocity spectra (E_{22}) have been normalized by their values at the minimum frequency. Spectral distributions were generated for all spanwise positions at

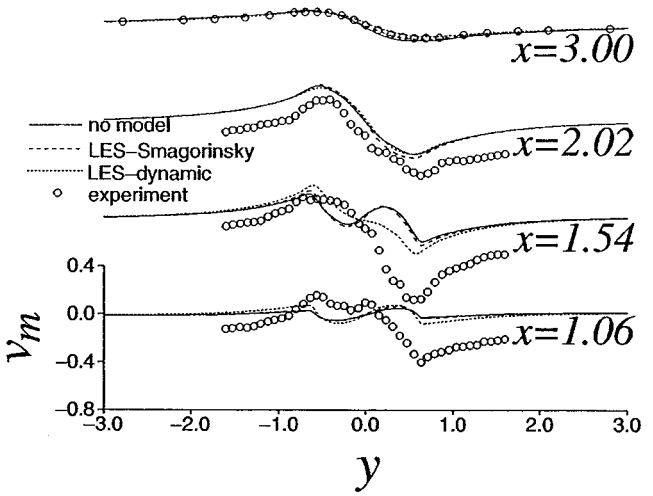

Figure 15. Spanwise averaged cylinder mean vertical velocity distributions in near wake.

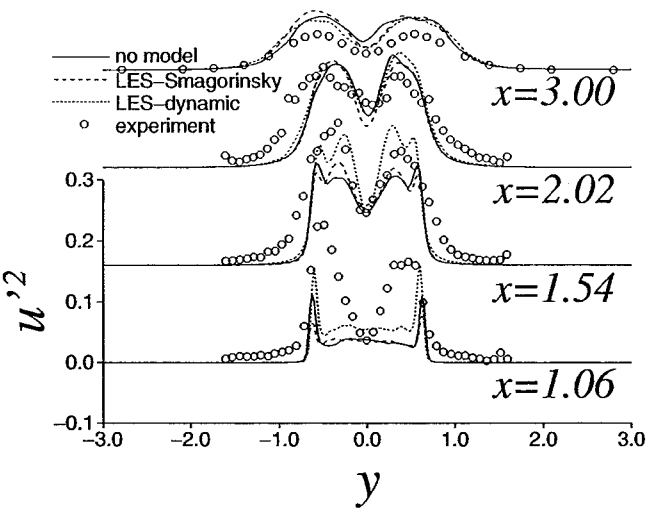

Figure 16. Spanwise averaged cylinder fluctuating streamwise velocity distributions in near wake.

each streamwise location. The resultant spectra were then spanwise averaged in order to produce the figures displayed here. Two discrete peaks are observed in the experimental vertical velocity spectra of Figure 19. The first peak corresponds to the primary Strouhal shedding frequency ($\omega/\omega_{St} = 1.0$), which is resolved by all computations. Also evident, is the second harmonic of the fundamental frequency [55], that is not well defined by any of the numerical solutions, especially far downstream where it was not possible to completely resolve all details of the complicated flow structure.

A comparison between the Smagorinsky and dynamic model eddy-viscosity coefficients is fashioned by the instantaneous spanwise averaged contours in Figure 20. The contours indicate

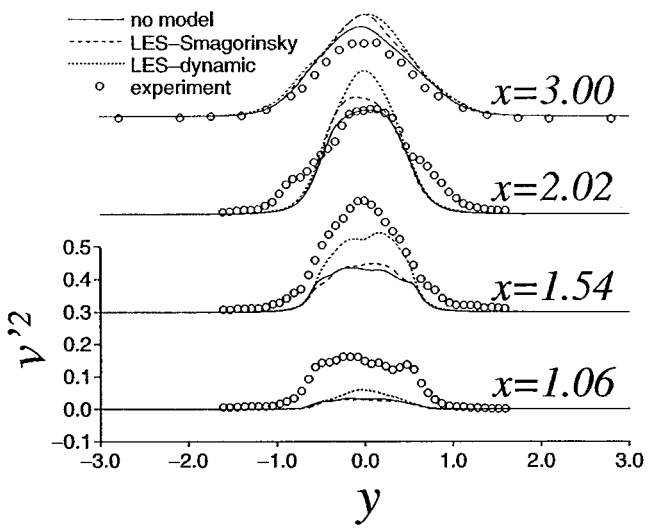

Figure 17. Spanwise averaged cylinder fluctuating vertical velocity distributions in near wake.

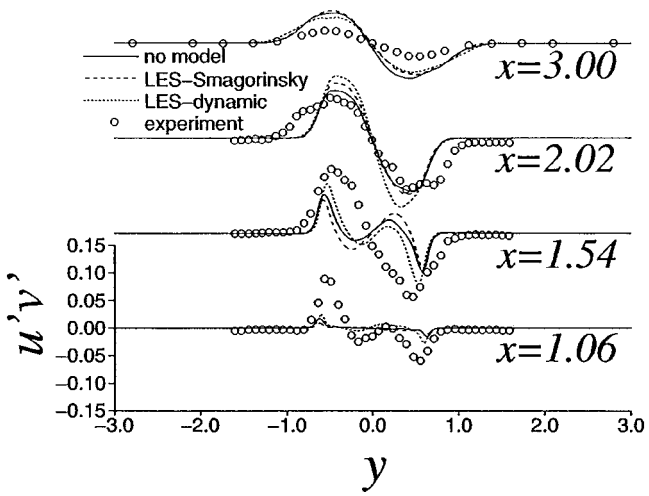

Figure 18. Spanwise averaged cylinder Reynolds shear stress distributions in near wake.

large eddy viscosity values in the separating shear layers of the Smagorinsky solution which are absent for the dynamic model, as was also observed by Beaudan and Moin [51]. Contours appearing in the figure have been normalized by the maximum eddy viscosity magnitude from each respective solution so that the comparison could be made with a consistent scale. Although the absolute maximum eddy viscosity within the domain is larger for the dynamic model, the high-valued regions are confined to the rotational structures of the wake, as opposed to the near-wall region.

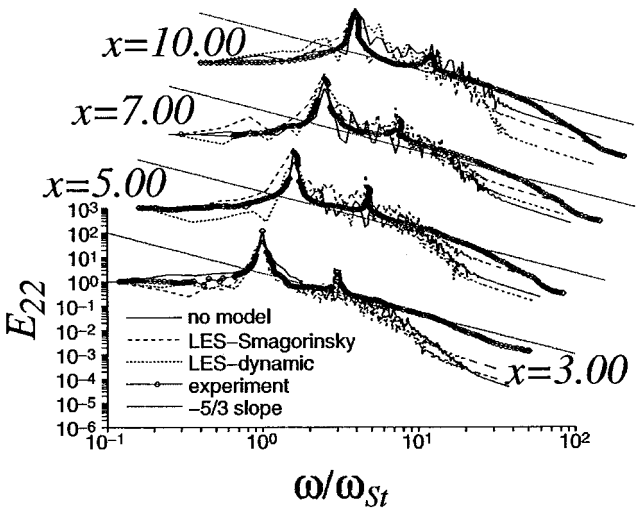

Figure 19. Spanwise averaged cylinder one-dimensional vertical velocity frequency spectra on wake centreline.

5. SUMMARY AND CONCLUSIONS

A numerical method has been described for performing large-eddy and direct-numerical simulation. The scheme employs a sixth-order non-dissipative compact finite-difference algorithm, which is used in conjunction with a tenth-order non-dispersive spatial filter. A series of validating computations were performed with time-implicit second-order temporal accuracy in order to demonstrate application of the method, as well as to evaluate the performance of subgrid-scale stress models for LES computations. These examples included the decay of compressible isotropic turbulence, turbulent channel flow, and the subsonic transitional flow past a circular cylinder.

The present no-model computations of decaying compressible turbulence were found to agree extremely well with a highly resolved spectral solution. LES calculations on coarser grids compared favourably with the no-model (DNS) result and with a previous spectral computation.

For the simulation of turbulent channel flow, both no-model and LES solutions gave reasonable results. This was due to the nature of the flow for which it was possible to resolve most of the significant flow scales, so that few differences were observed between the no-model and LES dynamic model solutions. Performance of the Smagorinsky model LES computation was slightly worse than that of the no-model or dynamic model simulations due to excessive dissipation.

The computation of a transitional cylinder flowfield illustrated the ability of the method to perform computations of wall-bounded flows on non-uniform curvilinear meshes. Extensive comparisons were carried out between experimental measurements and numerical simulations. The dynamic model LES computation provided superior performance in term of surface pressure, centreline velocity, and a number of time-mean quantities of interest. In addition, the

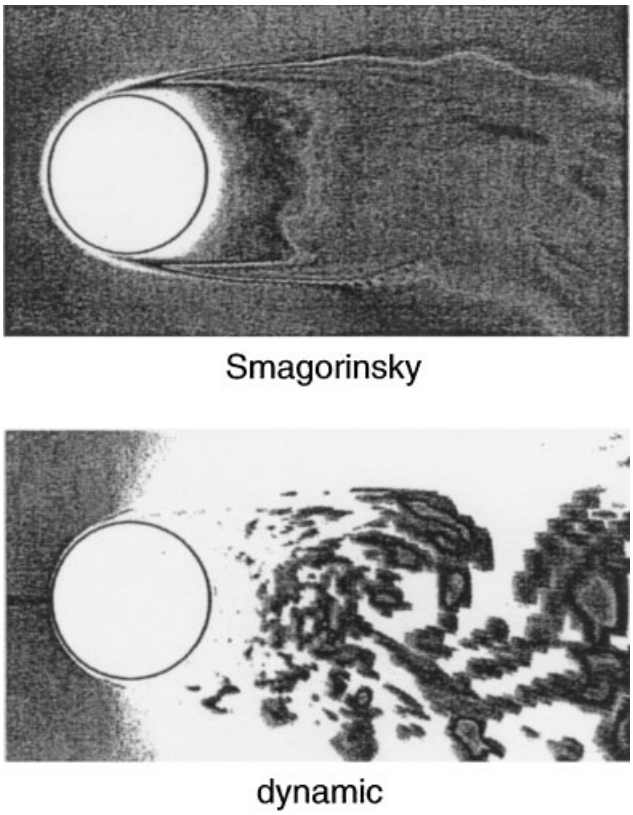

Figure 20. Instantaneous spanwise averaged cylinder eddy viscosity contours.

complex wake region appeared to be better defined by the dynamic model, as judged by both mean and fluctuating quantities over a majority of the measured domain.

The present scheme appears to provide a robust and accurate means for performing direct numerical and large-eddy simulations of practical flows. To further explore benefits of the scheme, applications at both higher Reynolds numbers and higher Mach numbers than those presented here should be attempted. Supersonic flows, including those with shock waves, should be considered.

ACKNOWLEDGEMENTS

The work presented here was sponsored by the U.S. Air Force Office of Scientific Research under Task 2307 AW and was monitored by L. Sakell. Computational resources were supported in part by a grant of supercomputer time from the U.S. Department of Defense Major Shared Resource Centers at Wright-Patterson AFB, OH, Vicksburg, MS, Stennis Space Center, MS, and Aberdeen Proving Ground, MD. The authors are grateful for conversations with D. V. Gaitonde and J. C. Tromp, and wish to acknowledge assistance provided by E. T. Spyropoulos.

REFERENCES

1. Smagorinsky JS. General circulation experiments with the primitive equations. *Monthly Weather Review* 1963; **91**(3):99–165.
2. Clark RA, Ferziger JH, Reynolds WC. Evaluation of subgrid-scale turbulence models using an accurately simulated turbulent flow. *Journal of Fluid Mechanics* 1979; **91**:1–16.
3. Deardorff JW. A numerical study of three-dimensional turbulent channel flow at large Reynolds numbers. *Journal of Fluid Mechanics* 1970; **41**:453–480.
4. Schumann U. Subgrid-scale model for finite-difference simulations of turbulent flows in plane channels and annuli. *Journal of Computational Physics* 1975; **18**(4):376–404.
5. Moin P, Kim J. Numerical investigation of turbulent channel flow. *Journal of Fluid Mechanics* 1982; **118**: 341–377.
6. Piomelli U, Moin P, Ferziger JH. Model consistency in large eddy simulation of turbulent channel flows. *Physics of Fluids* 1988; **31**(7):1884–1891.
7. Piomelli U, Cabot WH, Moin P, Lee S. Subgrid-scale backscatter in turbulent and transitional flows. *Physics of Fluids A* 1991; **3**(7):1766–1771.
8. Erlebacher G, Hussaini MY, Speziale CG, Zang TA. Toward the large-eddy simulation of compressible turbulent flows. *Journal of Fluid Mechanics* 1992; **238**:155–185.
9. Zang TA, Dahlburg RB, Dahlburg JP. Direct and large-eddy simulations of three-dimensional compressible Navier–Stokes turbulence. *Physics of Fluids A* 1992; **4**(1):127–140.
10. Ansari A, Strang WZ. Large-eddy simulation of turbulent mixing layers. *AIAA Paper* 96-0684, 1996.
11. Leith CE. Stochastic backscatter in a subgrid-scale model: plane shear mixing layer. *Physics of Fluids A* 1990; **2**(3):297–299.
12. Germano M, Piomelli U, Moin P, Cabot WH. A dynamic subgrid-scale eddy viscosity model. *Physics of Fluids A* 1991; **3**(7):1760–1765.
13. Moin P, Squires W, Cabot W, Lee S. A dynamic subgrid-scale model for compressible turbulence and scalar transport. *Physics of Fluids A* 1991; **3**(11):2746–2757.
14. Lilly DK. A proposed modification of the Germano subgrid-scale closure method. *Physics of Fluids A* 1992; **4**(3):633–635.
15. El-Hady NM, Zang TA, Piomelli U. Application of the dynamic subgrid-scale model to axisymmetric transitional boundary layer at high speed. *Physics of Fluids A* 1994; **6**(3):1299–1309.
16. Piomelli U. High Reynolds number calculations using the dynamic subgrid-scale stress model. *Physics of Fluids A* 1993; **5**(6):1484–1490.
17. Yang KS, Ferziger JH. Large-eddy simulation of turbulent obstacle flow using a dynamic subgrid-scale model. *AIAA Journal* 1993; **31**(8):1406–1413.
18. Ansari A. Performance of subgrid-scale models in predicting low- and moderate-Reynolds number wall-bounded flows. *AIAA Paper* 97-2011, 1997.
19. Zang Y, Street RL, Koseff JR. A dynamic mixed subgrid-scale model and its application to turbulent recirculating flows. *Physics of Fluids A* 1993; **5**(12):3186–3196.
20. Kravchenko AG, Moin P. On the effect of numerical errors in large eddy simulations of turbulent flows. *Journal of Computational Physics* 1997; **131**(2):310–322.
21. Ghosal S. Mathematical and physical constraints on large-eddy simulation turbulence. *AIAA Journal* 1999; **37**(4):425–433.
22. Gaitonde D, Shang JS, Young JL. Practical aspects of high-order accurate finite-volume schemes for electromagnetics. *AIAA Paper* 97-0363, 1997.
23. Visbal MR, Gaitonde DV. High-order-accurate methods for complex unsteady subsonic flows. *AIAA Journal* 1999; **37**(10):1231–1239.
24. Rizzetta DP, Visbal MR, Blaisdell GA. Application of a high-order compact difference scheme to large-eddy and direct numerical simulation. *AIAA Paper* 99-3714, 1999.
25. Yoshizawa A. Statistical theory for compressible turbulent shear flows, with the application to subgrid modelling. *Physics of Fluids* 1986; **29**(7):2152–2164.
26. Piomelli U, Liu J. Large-eddy simulation of rotating channel flow using a localized dynamic model. *Physics of Fluids* 1995; **7**(4):839–848.
27. Meneveau C, Lund TS, Cabot WH. A Lagrangian dynamic subgrid-scale model of turbulence. *Journal of Fluid Mechanics* 1996; **319**:353–385.
28. Wu X, Squires KD. Large eddy simulation of an equilibrium three-dimensional turbulent boundary layer. *AIAA Journal* 1997; **35**(1):67–74.
29. Beam R, Warming R. An implicit factored scheme for the compressible Navier–Stokes equations. *AIAA Journal* 1978; **16**(4):393–402.
30. Gordnier RE, Visbal MR. Numerical simulation of delta-wing roll. *AIAA Paper* 93-0554, 1993.
31. Jameson A, Schmidt W, Turkel E. Numerical solutions of the Euler equations by finite volume methods using Runge–Kutta time stepping schemes. *AIAA Paper* 81-1259, 1981.

32. Pulliam TH, Chaussee DS. A diagonal form of an implicit approximate-factorization algorithm. *Journal of Computational Physics* 1981; **39**(2):347–363.
33. Visbal MR, Rizzetta DP. Large-eddy simulation on curvilinear grids using compact differencing and filtering schemes. *Journal of Fluids Engineering* 2003; **124**(4):836–847.
34. Lele SA. Compact finite difference schemes with spectral-like resolution. *Journal of Computational Physics* 1992; **102**(1):16–42.
35. Gaitonde D, Visbal MR. High-order schemes for Navier–Stokes Equations: algorithm and implementation into FDL3DI. *AFRL-VA-WP-TR*-1998-3060, 1998.
36. Gordnier RE. Computation of delta-wing roll maneuvers. *AIAA Paper* 93-2975, 1993.
37. Visbal MR. Computational study of vortex breakdown on a pitching delta wing. *AIAA Paper* 93-2974, 1993.
38. Visbal MR. Onset of vortex breakdown above a pitching delta wing. *AIAA Journal* 1994; **32**(8):1568–1575.
39. Visbal M, Gaitonde D, Gogineni S. Direct numerical simulation of a forced transitional plane wall jet. *AIAA Paper* 98-2643, 1998.
40. Rizzetta DP, Visbal MR, Stanek MJ. Numerical investigation of synthetic jet flowfields. *AIAA Journal* 1999; **37**(8):919–927.
41. Fyfe DJ. Economical evaluation of Runge–Kutta formulae. *Mathematics of Computation* 1966; **20**(95): 392–398.
42. Boris JP, Grinstein FF, Oran ES, Kolbe RJ. New insights into large eddy simulation. *Fluid Dynamic Research* 1992; **10**(4–6):199–227.
43. Fureby C, Grinstein FF. Monotonically integrated large eddy simulation. *AIAA Journal* 1999; **37**(5):544–556.
44. Spyropoulos ET, Blaisdell GA. Evaluation of the dynamic model for simulations of compressible decaying isotropic turbulence. *AIAA Journal* 1996; **34**(5):990–998.
45. Ristorcelli JR, Blaisdell GA. Consistent initial conditions for the DNS of compressible turbulence. *Physics of Fluids A* 1997; **9**(1):4–6.
46. Kreplin H-P, Eckelmann H. Behavior of the three fluctuating velocity components in the wall region of a turbulent channel flow. *Physics of Fluids* 1979; **22**(7):1233–1239.
47. Eckelmann H. The structure of the viscous sublayer and the adjacent wall region in a turbulent channel flow. *Journal of Fluid Mechanics* 1974; **65**:439–459.
48. Pai SI. On turbulent flow between parallel plates. *Journal of Applied Mechanics* 1953; **20**:109–114.
49. Kim J, Moin P, Moser R. Turbulent statistics in fully developed channel flow at low Reynolds number. *Journal of Fluid Mechanics* 1987; **177**:133–166.
50. Okong'o N, Knight DD. Compressible large eddy simulation using unstructured grids: channel and boundary layer flows. *AIAA Paper* 98-3315, 1998.
51. Beaudan P, Moin P. Numerical experiments on the flow past a circular cylinder at sub-critical Reynolds number. *Report No.* TF-62, Department of Mechanical Engineering, Stanford University, 1994.
52. Mittal R, Moin P. Suitability of upwind-biased finite difference schemes for large-eddy simulation of turbulent flows. *AIAA Journal* 1997; **35**(8):1415–1417.
53. Kravchenko AG, Moin P. B-Spline methods and zonal grids for numerical simulations of turbulent flows. Flow Physics and Computation Division. *Report No.* TF-73, Department of Mechanical Engineering, Stanford University, 1998.
54. Jordan SA, Ragab, SA. A large-eddy simulation of the near wake of a circular cylinder. In *Proceedings of the 1994 International Mechanical Engineering Congress and Exposition,* vol. 203. Turbulence in Complex Flows American Society of Mechanical Engineers, Fluids Engineering Division. ASME: New York, 1994; 1–9.
55. Ong L, Wallace J. The velocity field of the turbulent very near wake of a circular cylinder. *Experiments in Fluids* 1996; **20**(6):441–451.